INTERNATIONAL JOURNAL OF AUTOMOTIVE AND MECHANICAL ENGINEERING (IJAME)
ISSN: 2229-8649 e-ISSN: 2180-1606
VOL. 19, ISSUE 1, 9563 – 9576
DOI: https://doi.org/10.15282/ijame.19.1.2022.19.0738

ORIGINAL ARTICLE

Numerical Simulation Approach to Investigate the Effects of External Modifications in Reducing Aerodynamic Drag on Passenger Vehicles

M. Sadat[1,*], N. Albab[1], F. Chowdhury[1] and M.M.A. Khan[2]

[1]Department of Mechanical Engineering, Shahjalal University of Science and Technology, Kumargaon, Sylhet – 3114, Bangladesh
[2]Department of Industrial and Production Engineering, Shahjalal University of Science and Technology, Kumargaon, Sylhet – 3114, Bangladesh

ABSTRACT – This study used a numerical simulation approach to examine the effects of external modifications in reducing aerodynamic drag on passenger vehicles. During the simulation, modifications included reducing mirror size by replacing the side mirrors with cameras and covering the wheel area. The resulting changes in drag force for different combinations of modifications were compared with a conventional baseline model to determine the most aerodynamic configuration. The study found that side view cameras reduced drag forces by almost 2.6% due to their smaller frontal areas and improvement in the overall aerodynamics of the vehicle. Besides, an increase in wheel coverage decreased the drag causing up to 2.7% of drag force reduction for a wheel with an 87% coverage area. This is because of the reduction in wake formation caused by the wheel rims. Finally, using a combination of smaller cameras and wheels with larger coverage areas resulted in a maximum drag reduction of about 4.3%.

ARTICLE HISTORY
Received: 25th Mar 2021
Revised: 21st Jan 2022
Accepted: 14th Mar 2022

KEYWORDS
Aerodynamic drag;
Side view mirrors;
Wheel covers;
Numerical simulation;
Drag reduction

INTRODUCTION

The automobile industry is one of the key contributors to global warming and other adverse climate changes. Therefore, to minimize the environmental impact of transportation, it is vital for automakers to ensure that their vehicles are highly energy efficient. One way of achieving this goal is influencing the vehicle's aerodynamics to minimize the power needed to drive the vehicle. For this reason, aerodynamics has received increasing attention over the last five decades in the experimental and practical field of vehicle research, mainly due to its effects on fuel economy and performance. The most common way to improve the aerodynamics of vehicles is by controlling their exterior shape. However, two lesser-known modifications that have gained increased attention in recent years are side-view mirror replacing cameras and aerodynamic wheel covers. Wheels contribute to about 25% of the total drag force of a vehicle [1]. In an experimental study on isolated generic and production wheels, the influence of geometry, camber, and brake disc on wheel aerodynamics was observed by Haag et al. [2]. Berg and Brandt [3] investigated the aerodynamic effect of different wheel designs. Both experimental and numerical tools were used to evaluate the importance of different wheel parameters. It was found that the coverage area was the most critical design parameter of the wheel. The rim cover and the depth of the center were also found to be significant parameters. They also concluded that limiting outflow from the wheel helps reduce drag.

Waschle [4] did an experimental and numerical analysis on the influence of wheel rotation on the drag coefficient. He showed that wheel rotation reduces the drag of the whole vehicle body. The reason for this drag reduction was the changed interaction between the wakes of the rear wheels and the wake of the car. Koitrand et al. [5] applied experimental and numerical methods to examine the effect of wheel aerodynamics on a sedan. A noticeable decrease in drag was observed with a fully covered wheel compared to a conventional wheel. The results show a connection between drag reduction and covering towards the perimeter of the wheels. A similar numerical study on wheel aerodynamics and its effect on the drag coefficient was conducted by Bolzon et al. [6] using both stationary and rotating wheels. The effects of wheel rotation, rim coverage area, fan spokes, spoke sharpness, and tread pattern on a passenger vehicle's flow field and drag coefficient were investigated. He found that increasing the rim coverage area reduces the drag. Furthermore, rounding the spoke edges was observed to have reduced the drag under rotating conditions.

The aerodynamics of side mirrors is one of the newest areas of interest in vehicle design. The side-view mirrors of a car increase the drag coefficient by 2-7% [7]. Studies conducted by Ehlert et al. [8] described a two-step process to develop a mirror shape that meets both wind noise and aerodynamic objectives. The relationships between wind noise and drag responses revealed that sail-mounted mirrors have performance range limitations. Therefore, a door-mounted mirror design was chosen, and the shape was then optimized using response surface methods and optimization techniques. Alam and Mahmood [9] compared the drag forces acting on a flat back circular side view mirror and a hemispherical backside view mirror in fuel consumption. The authors reported that the maximum reduction due to design change from flat back to hemispherical back was 29.3 liters per year when the car traveled at 120 km/h. Olsson [10] designed and optimized side view mirrors by modifying various features such as changing edge radius, inclinations, and adding gutters. The drag contribution from the optimized mirror was reduced by 12 drag counts from the standard model. The wind

*CORRESPONDING AUTHOR | M. Sadat | ✉ saadatmostofa@gmail.com

tunnel tests also show a decrease in drag contribution for the modified mirrors, but not as large as the CFD simulations. He concluded that simulations of side mirrors have an uncertainty of a few drag counts and certain inconsistencies but can capture trends of changes. Magazoni et al. [11] used optimization techniques to provide an aerodynamic shape improvement of the side-view mirror and its effect on a hatchback vehicle's drag coefficient. The optimization solver is used to improve the surface of the view mirror to decrease its drag force. The results show a decrease in a drag coefficient of 8 drag counts for the view mirror's optimized surface. Ipci [12] investigated the impact of side-view mirrors and side-view cameras on the drag coefficient of a bus model using computational fluid dynamics (CFD). The drag coefficients were 0.539 and 0.521 for the bus with side-view mirrors and cameras, respectively.

Buscariolo and Rosilho [13] performed a CFD-based study to reduce the drag coefficient using cameras as alternatives to replacing the side-view mirrors. In their study, two types of camera housings were proposed to substitute a regular side-view mirror, one of which was designed based on an airfoil profile attached to a cylindrical-shaped camera. As a result, the drag coefficient was reported to have reduced by 0.5%. McWha [15] performed experimental studies on a heavy-duty truck where the side mirrors were replaced with a four-camera monitoring system. The net decrease in drag coefficient was 20 drag coefficient. He also estimated the net fuel savings per year as approximately 1172 liters. Korkut and Goren [16] performed numerical simulations on the aerodynamics of solar and electric-powered prototype racing cars using side-view cameras. Using cameras made the electric vehicle 15.05% more efficient and the solar car 18.28% more efficient aerodynamically.

The literature shows that a reduction in drag force is made possible by bringing various modifications to the vehicle wheel and its side-view mirrors. In addition, replacing the side-view mirrors with side-view cameras can cause a reduction in the drag coefficient. However, as far as authors' knowledge, simultaneous modification of wheel covers and side-view mirrors or side-view cameras and their effects on the drag coefficient has not been explored yet. Therefore, this study focuses on the drag reduction potential for simultaneously modifying wheel covers and side-view cameras in a passenger vehicle. Furthermore, it tries to determine a combination of modified components under consideration that would minimize the drag.

METHODOLOGY

Theory

The formula that is used to define the aerodynamic drag force is written as:

$$F = (1/2)\,\rho V^2 C_D A \quad (1)$$

Where F is the aerodynamic drag, A is the projected frontal area, C_D is the drag coefficient and $(1/2)\rho V^2$ is the dynamic pressure of the fluid. C_D is a dimensionless number representing the resistance to fluid flow due to the shape of the body. The dynamic pressure is constant for air at a fixed relative velocity under Mach 0.3 (103 m/s). It can be observed that, for constant dynamic pressure, the drag force is directly proportional to C_D and A. Therefore, drag forces can be reduced by decreasing the drag coefficient, C_D or the frontal area, A of the vehicle, or both.

In our investigation, the application of wheel cover is expected to reduce the turbulence of wheel rims and allow air to smoothly pass over the wheels, reducing the C_D and, therefore, the resultant drag force. On the other hand, side view cameras are expected to reduce drag because of their smaller frontal area than traditional mirrors. In addition to that, the drag coefficient is subject to alteration due to the change in the vehicle's overall shape.

Geometry

As shown in Figure 1(a) and 1(b), a vehicle's three-dimensional model was generated using the SOLIDWORKS software. The basic shape of the vehicle is based on the side profile of a modern slanted-back SUV. A simplified car model was created by cleaning up the geometric details irrelevant to the analysis. This was done in order to reduce computational costs without affecting accuracy.

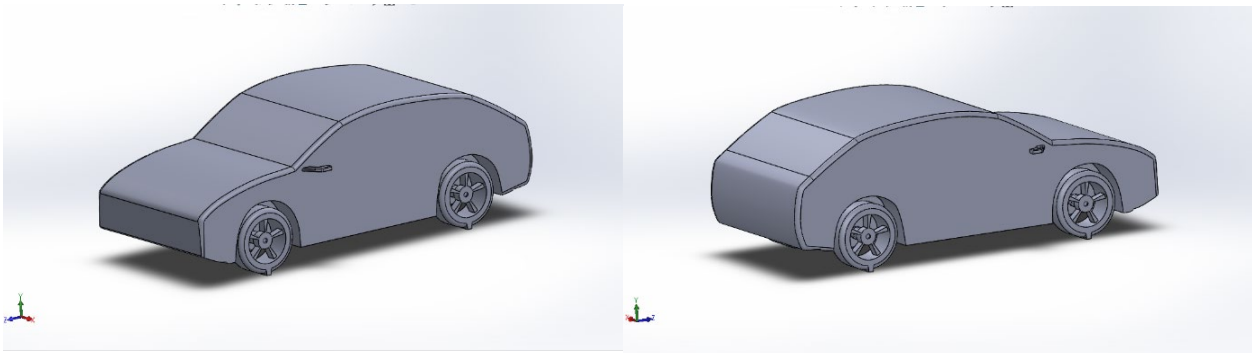

Figure 1. Vehicle model (a) front and (b) rear 3/4ths view

Two camera designs were conceived. The first design is referred to as C1, and the second design is referred to as C2. For comparison, a generic side view mirror (denoted as M) was created separately. The frontal areas of M, C1, and C2

are 190 cm^2, 86.4 cm^2, and 20.6 cm^2, respectively. 3D models of the conventional mirror (M) and the cameras (C1 and C2) have been illustrated in Figures 2(a) to 2(c). It is worth mentioning that the dimensions of side-view cameras used in the production cars vary widely in their length and height. In this study, the length of housings for C1 and C2 were 0.9 and 0.33 times the length of the conventional mirror, respectively. On the other hand, the height of the housings for C1 and C2 were 0.4 and 0.25 times the mirror's height, respectively. Furthermore, the shape of their cross-section and the frontal area considered in this study was rectangular.

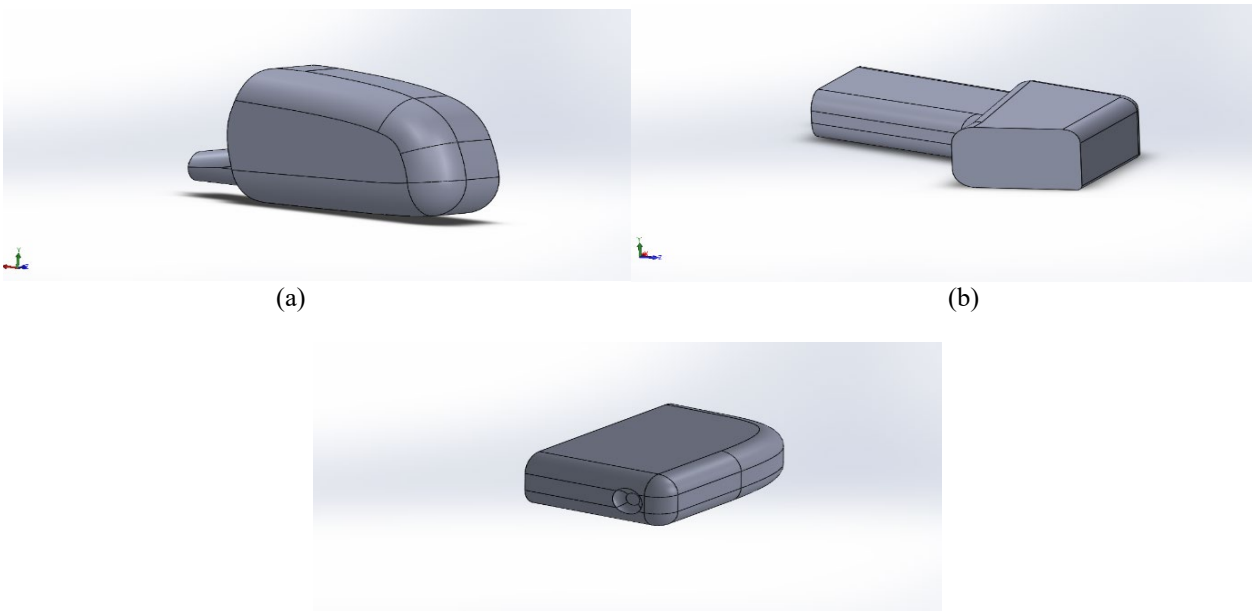

(a) (b)

(c)

Figure 2. 3D model of (a) conventional mirror, M, (b) Camera C1, and (c) Camera C2.

Three designs of the wheel were used in this study. The first wheel design is considered the base design with a coverage area of 25% of the whole rim. The second and third wheel designs are based on the first wheel, in which the central circle is expanded to obtain a total coverage area of 66% and 87%, respectively. The wheels are designated respectively as W1, W2, and W3, and their 3D models have been illustrated in Figures 3(a) to 3(c).

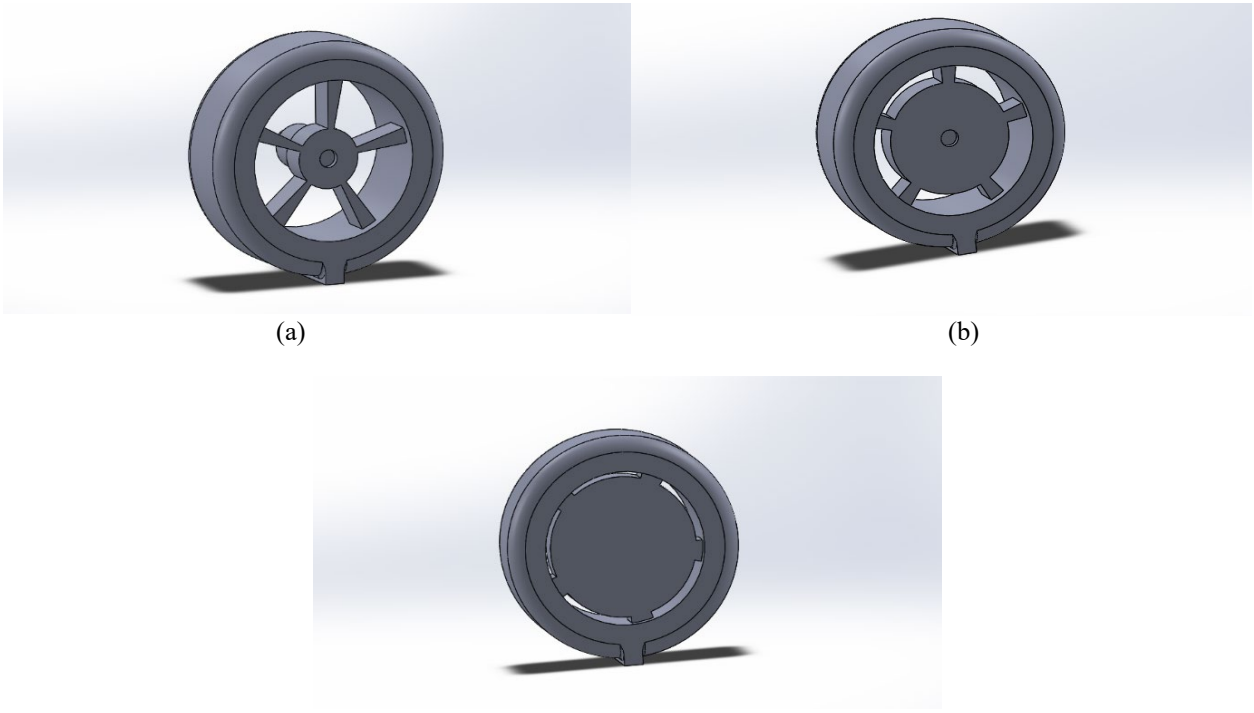

(a) (b)

(c)

Figure 3. 3D model of the wheel with a coverage area of (a) 25% (W1), (b) 66% (W2) and (c) 87% (W3).

The vehicle's configuration being tested is denoted in this manner: the vehicle equipped with a conventional mirror (M) and the base wheel design (W1) was designated as M-W1. Similarly, other configurations are denoted as C2-W1, M-W3, etc. However, in this study, M-W1 is considered the default configuration as it includes the conventional mirror and wheels.

Computational Domain

The computational domain, shown in Figure 4, is a rectangular box with a cross-section of 14×14 m. The vehicle's position is such that the inlet is five car lengths in front of the vehicle and the outlet is seven car lengths from the vehicle's rear. The inlet velocity was defined at 40 m/s and outlet pressure at zero gauge pressure. Thus, the inlet is along the positive Z-axis. As the model is symmetric about the ZY-plane, the calculation was done on only one-half of the model using symmetric boundary conditions to reduce the computational resource needed while providing the same accuracy as a full model analysis.

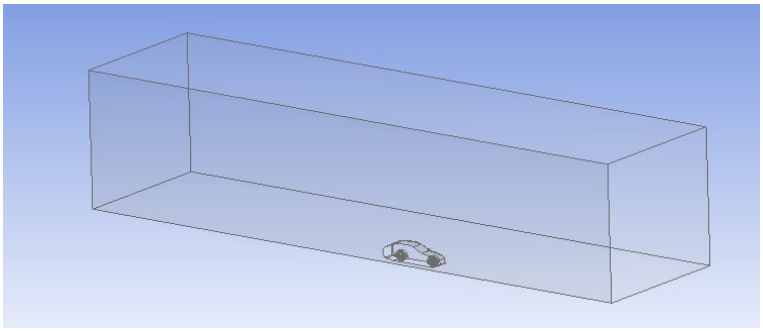

Figure 4. Computational domain.

Discretization Setup

As shown in Figure 5, a mixture of unstructured tetrahedral and prism cells was used for meshing. Five layers of prismatic cells were used as an inflation layer in the wall regions, while the rest of the domain was filled with tetrahedral cells. The inflation generating method was a First Aspect Ratio of 5 and a growth rate of 20% to ensure a good transition in terms of cell volume at the interface between the prismatic layers and the tetrahedral region. The average y+ value was 160, and therefore, the corresponding first layer height is 1.6 mm. The y+ distribution is shown in Figure 6. The vehicle's body, wheels, and mirrors/cameras had a surface mesh of 50 mm, 10 mm, and 2 mm, respectively.

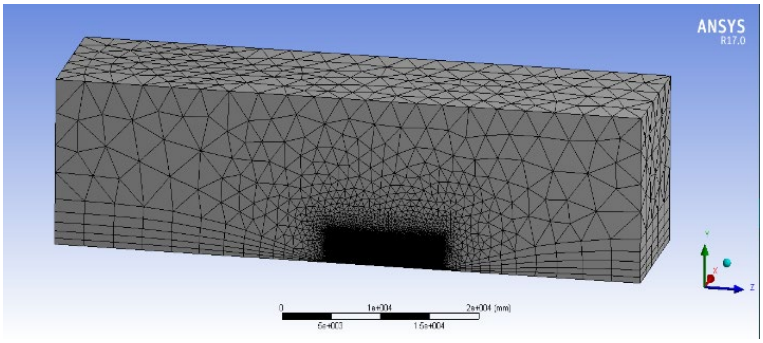

Figure 5. Types of mesh used in the simulation.

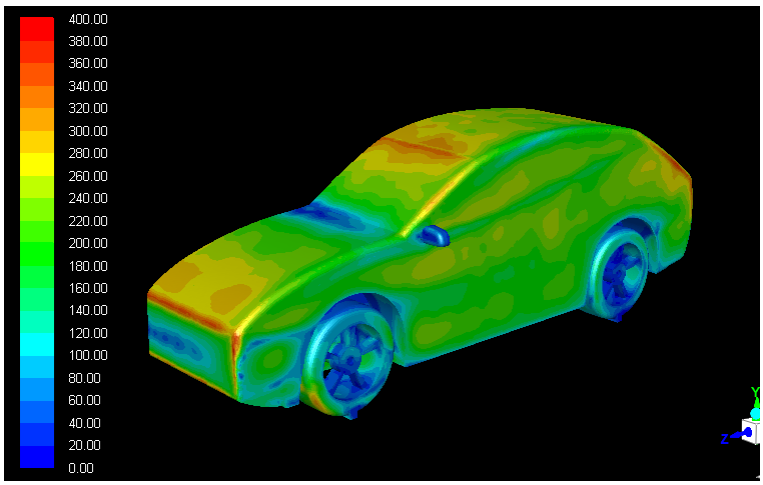

Figure 6. y+ distribution over the vehicle surface.

As shown in Figure 7 to 9, a refinement box of 70 mm elements was used to create fine mesh around the vehicle's vicinity, where interaction with air occurs. Coarse mesh sizing was used at the regions far away from the vehicle in the free stream region. Two additional refinement boxes of 50 mm elements – one in the gap between the vehicle and road and another in the body's wake region were used. These boxes predict better the complex flow phenomena and adverse pressure gradients in those regions, increasing the simulation's accuracy and reliability. The mesh count was about 4 million elements.

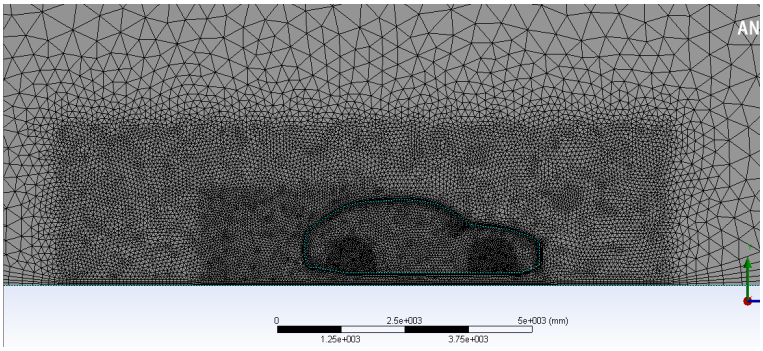

Figure 7. Refined mesh around the vehicle.

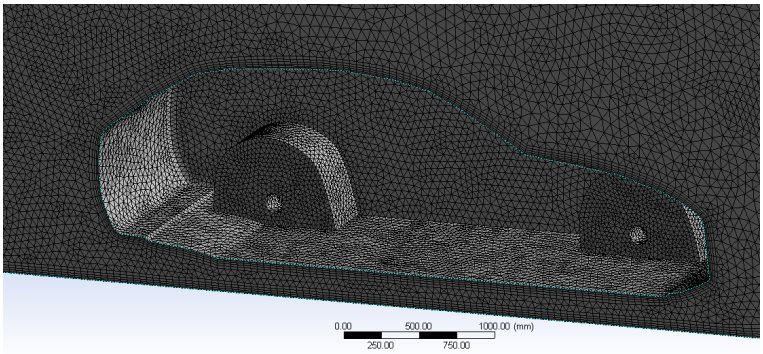

Figure 8. Close-up view of the surface mesh.

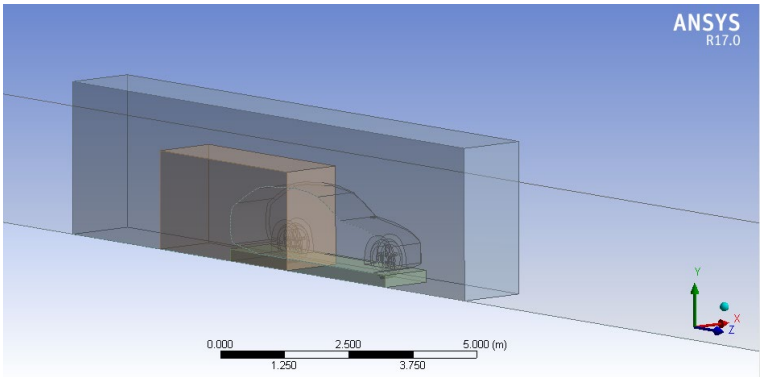

Figure 9. Mesh refinement boxes.

Solver Settings

The RANS (Reynold's Averaged Navier-Stokes) equations of mass, continuity, and energy are solved in a steady-state, pressure-based solver to compute flow variables. The RANS equation for a stationary flow of an incompressible Newtonian Fluid can be written in Cartesian coordinates as:

$$\rho\bar{u}_j\frac{\partial\bar{u}_i}{\partial x_j}=\rho\bar{f}_i+\frac{\partial y}{\partial x_j}\left[-\bar{p}\delta_{ij}+\mu\left(\frac{\partial\bar{u}_i}{\partial x_j}+\frac{\partial\bar{u}_j}{\partial x_i}\right)-\rho\overline{\acute{u}_i\acute{u}_j}\right] \tag{2}$$

The turbulence is modeled using a Realizable k-Ɛ turbulence model with non-equilibrium wall functions. The transport equations of the Realizable k-ϵ model are –

$$\begin{aligned}\frac{\partial}{\partial t}(\rho k)+\frac{\partial}{\partial x_j}(\rho k u_j)&=\frac{\partial}{\partial x_j}\left[(\mu+\frac{\mu_t}{\sigma_k})\frac{\partial k}{\partial x_j}\right]+P_k+P_b-\rho\epsilon-Y_M+S_k\\ \frac{\partial}{\partial t}(\rho\epsilon)+\frac{\partial}{\partial x_j}(\rho\epsilon u_j)&=\frac{\partial}{\partial x_j}\left[(\mu+\frac{\mu_t}{\sigma_\epsilon})\frac{\partial\epsilon}{\partial x_j}\right]+\rho C_1 S\epsilon-\rho C_2\frac{\epsilon^2}{k+\sqrt{\nu\epsilon}}+C_{1\epsilon}\frac{\epsilon}{k}C_{3\epsilon}P_b+S_\epsilon\end{aligned} \tag{3}$$

The air density was set constant at 1.225 kg/m^3 and viscosity 1.7894×10^{-05} kg/m-s. The simulations were done with AMD Ryzen 5 3400G CPU with a clock speed of 3.7 GHz and 16GB RAM. The average time for each simulation was 12 hours. The boundary conditions used in the simulations are shown in Table 1.

Table 1. Boundary conditions used in the simulations.

Constants	Boundary conditions
Inlet velocity	40 m/s
Inlet turbulence intensity	1%
Outlet gauge pressure	0 Pa
Outlet turbulence intensity	5%
Wall zones	No-slip (bottom), symmetry (top, left, right)

VALIDATION

In this study, the flow over the Ahmed body [14] was used to validate the numerical solutions as it is a generic bluff body widely used for studying the external aerodynamics of vehicles. This body consists of a parallelepiped with rounded edges at the front and a slanted face at the rear. Although having a simplified geometry, the airflow around the Ahmed body retains the essential flow characteristics around a passenger vehicle. Therefore, it is often utilized to describe the turbulent flow field around a car-like bluff body shape.

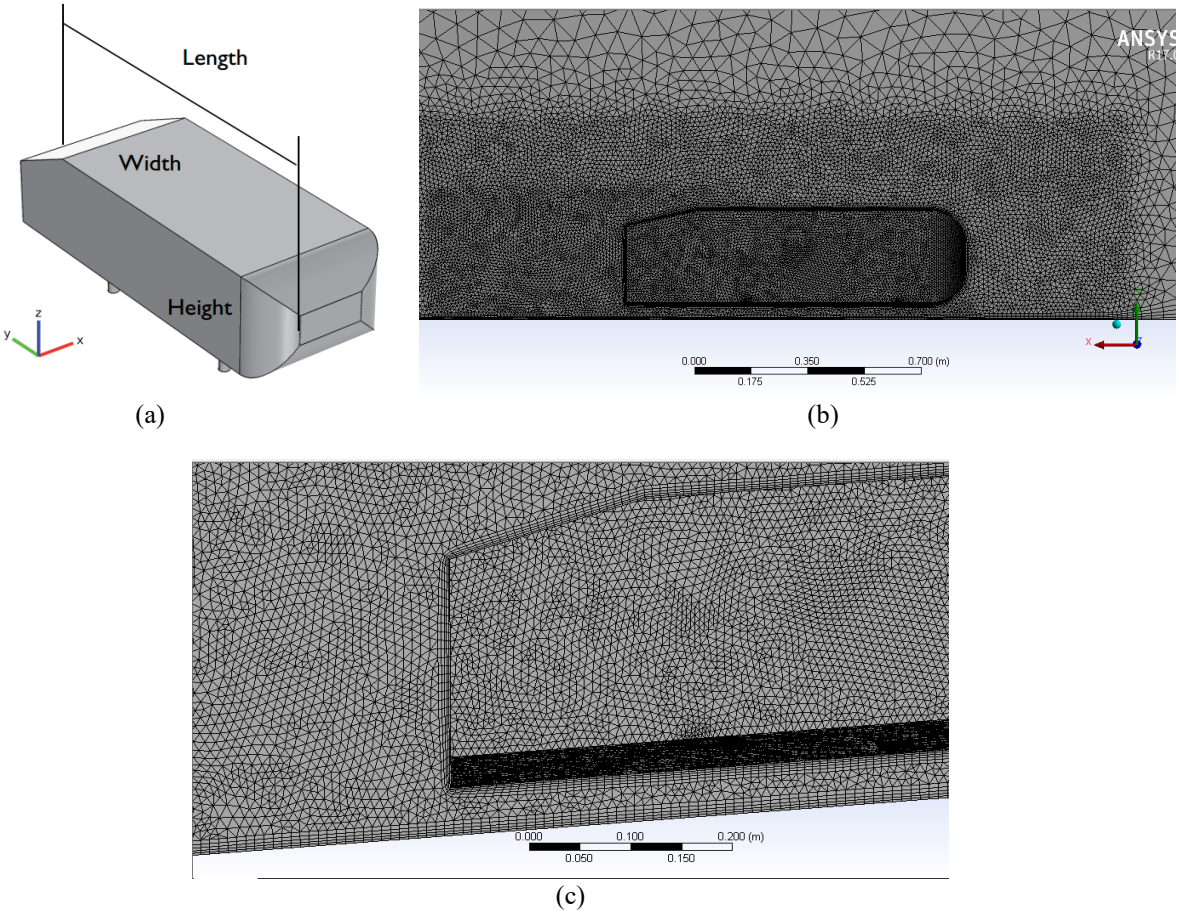

(a) (b)

(c)

Figure 10. (a) Ahmed Body, (b) refined mesh around Ahmed body and (c) close up view of the mesh.

Table 2. Ahmed body validation test with various slant angles.

Slant angle (degree)	C_d (experimental)	C_d(simulation)	% of error
12.5	0.230	0.243	5.7%
20	0.250	0.261	4.4%
25	0.285	0.288	1.1%

The drag coefficient of Ahmed Body for various slant angles has been determined by researchers experimentally and is included in Table 2. These results serve as a benchmark to validate modern-day numerical studies. In this study, drag

coefficients for Ahmed body with slant angles of 12.5, 20, and 25 degrees were numerically determined and compared with experimental values, as shown in Table 2.

From our tested configurations, the component drag of a 12.5 degree slant is found in Ahmed [14]. The component drags are defined as C_K^*, C_S^*, C_B^*, which are the pressure drag coefficients of the front, the slanted back, and the vertical back faces, respectively, and $C_P^* = C_K^* + C_S^* + C_B^*$. C_R^* is the skin friction drag coefficient. The component drags from the experimental and simulation results are given below in Table 3.

Table 3. Ahmed body 12.5 degree angle component drag coefficients.

Component	Experimental	Simulation	Difference
C_K^*	0.016	0.017	6.25%
C_S^*	0.037	0.039	5.4%
C_B^*	0.122	0.123	0.82%
C_P^*/C_d	0.76	0.74	-2.63%
C_R^*/C_d	0.24	0.26	8.33%

Besides, Ahmed [14] also points out that the pressure drag is close to 80% or higher than the total drag. In our simulations, the pressure drag is 80% for a 12.5 degree slant angle, 82% for a 20 degree slant, and 83% for a 25 degree slant angle. The results from simulations show good agreement with the experimental values with a low percentage of error (<10%). Therefore, the simulation approach considered is valid and can be used for further analysis.

RESULTS AND DISCUSSION

The term 'drag counts' was used to simplify the way of comparing C_d values. For example, in this study, one drag count is 0.001 C_d. To better understand the effects of the configuration changes, the simulations were conducted in two separate cases.

Mesh Sensitivity

First, the effects of the default vehicle configuration (M-W1) were simulated. Its data served as the baseline value with which other configurations were compared. Next, the simulations were performed with varying refinement settings to test grid independence. The results of mesh sensitivity are shown in Table 4. The results show that the maximum deviation of the tests is only 3.6%, with the deviation of Mesh C and D dropping to only 0.25%. Due to this slight variance over a wide range of mesh counts, the results are assumed to be mostly grid-independent. Besides, it was observed from the work of Olsson [10] that uncertainty of a few drag counts exists in simulations related to side mirrors. Considering this fact, Mesh E was selected because of its highest accuracy to reduce this uncertainty as much as possible.

Table 4. Mesh sensitivity outcomes.

	A	B	C	D	E
No. of cells (millions)	2.3	2.5	2.7	3	4
C_d	0.428	0.419	0.414	0.414	0.413

Case 1 – Changing Mirrors/Cameras while Keeping the Default Wheel Unchanged

The vehicle was fitted with two different camera designs (C1 and C2) for the default wheel (W1) and simulated in the first case. The resulting data are tabulated and compared in Table 5 and Figure 11. In addition, as the frontal area varies with the size of the camera used, the product of drag coefficient and frontal area (C_d.A) has also been included so that the change in drag with the camera can be explained more accurately.

Table 5. Variation in drag force for replacing the mirror with a camera housing of different sizes.

Configuration	Drag coefficient	C_d.A (A in m^2)	Drag force (N)	Reduction
M-W1 (baseline)	0.413	1.192	584	-
C1-W1	0.409	1.172	574	1.7%
C2-W1	0.407	1.162	569	2.6%

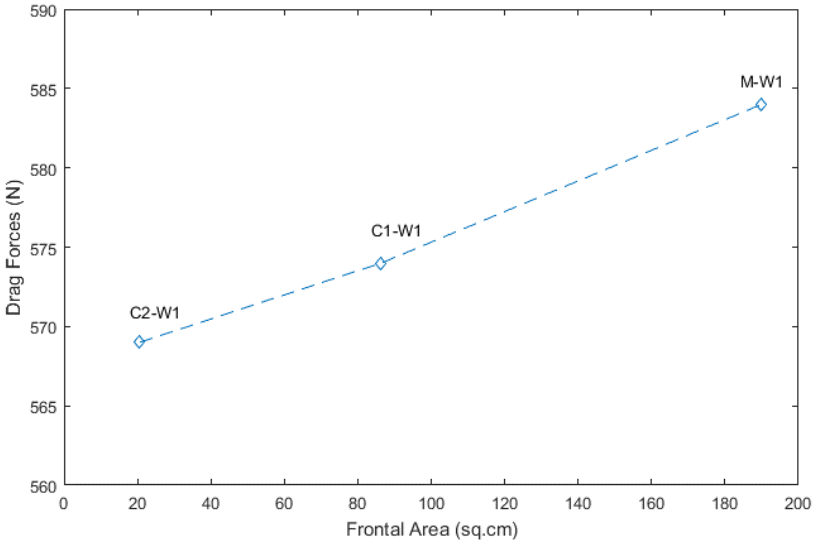

Figure 11. Change in drag force with mirror/camera frontal area.

From Figure 11 and Table 5, it is observed that the mirror generates the highest drag, and the drag force decreases with equipping smaller cameras. These results confirm our predictions that decreasing the frontal area results in reduced drag. From Figure 12(a) to 12(c), it can be seen that the high static pressure zone (marked in red) is substantially smaller for the cameras than the mirror, which indicates lesser drag.

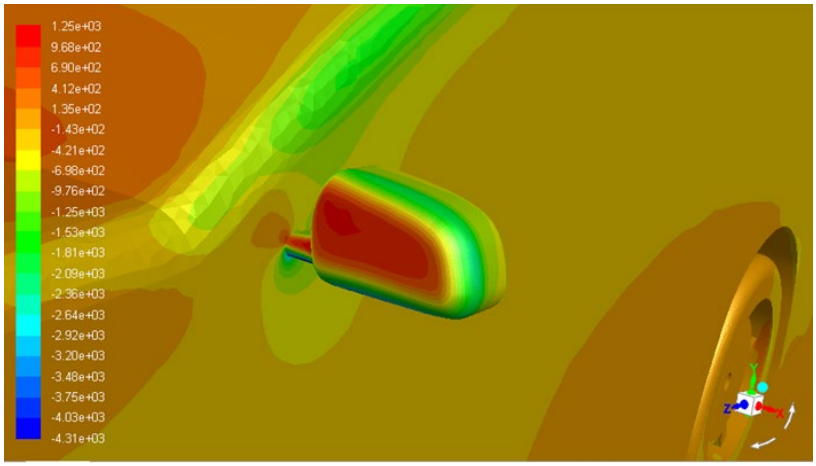

(a)

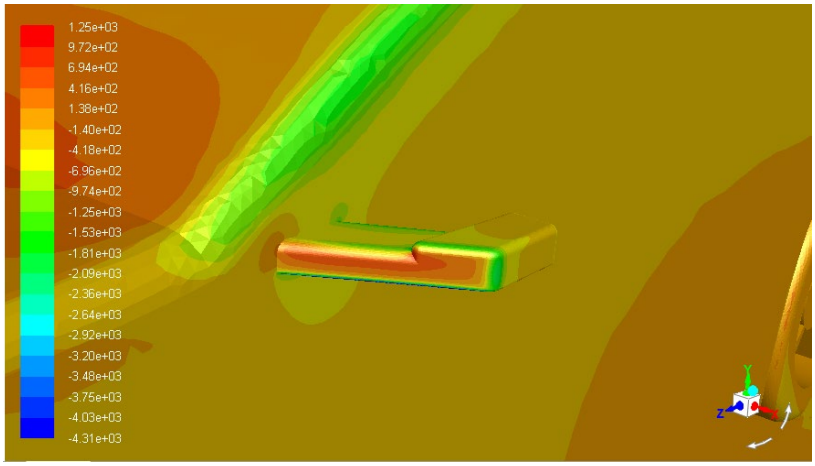

(b)

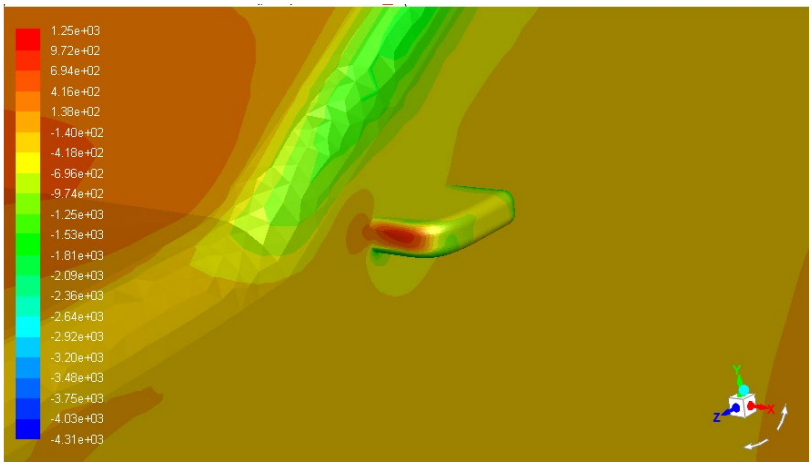

(c)

Figure 12. Contour of static pressure on (a) mirror, (b) C1, and (c) C2.

Figure 13(a) to 13(c) shows the wake structure formed by the mirror and the cameras. As expected, the wake formed by the mirror is substantially larger than the cameras. Among the two cameras, C2 has the smallest wake. However, a comparatively large wake is formed close to its base along the vehicle's body, which explains the minimal difference between the drag coefficient of C1 and C2 (i.e., 0.409 and 0.407, respectively).

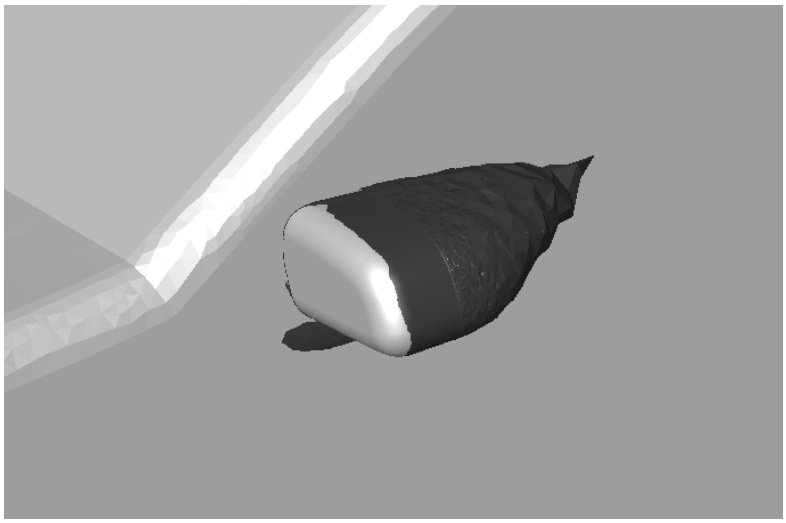

(a)

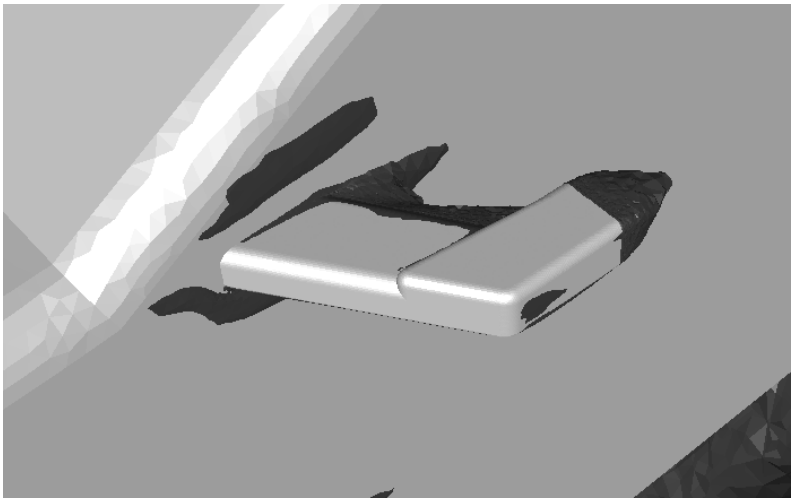

(b)

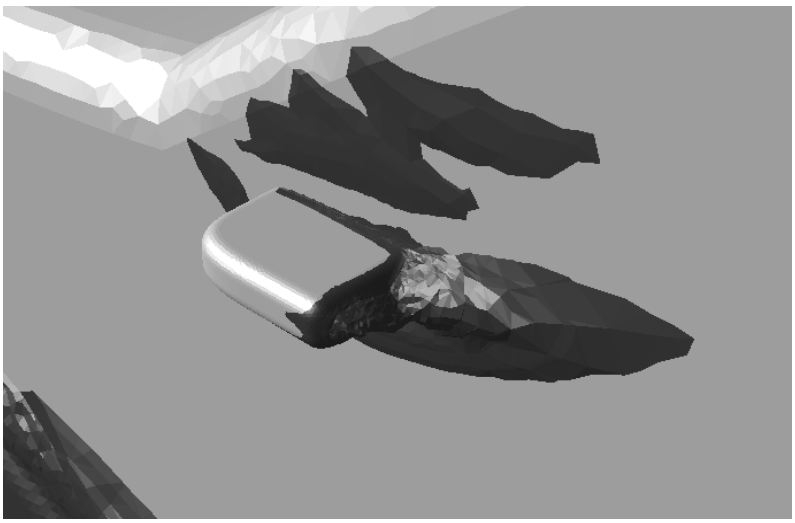

(c)

Figure 13. Wake formation for (a) conventional mirror, (b) C1, and (c) C2.

Finally, Figure 14(a) to 14(c) shows the distribution of static pressure on the back of the vehicle. Although they look very similar, some differences can be seen in the lower left part of the back. A higher pressure region expands in size when switching from M-W1 to C1-W1 and expands further (albeit slightly) in C2-W1. This scenario signifies a higher base pressure in the back due to smaller cameras, resulting in lesser pressure drag and lower drag coefficient.

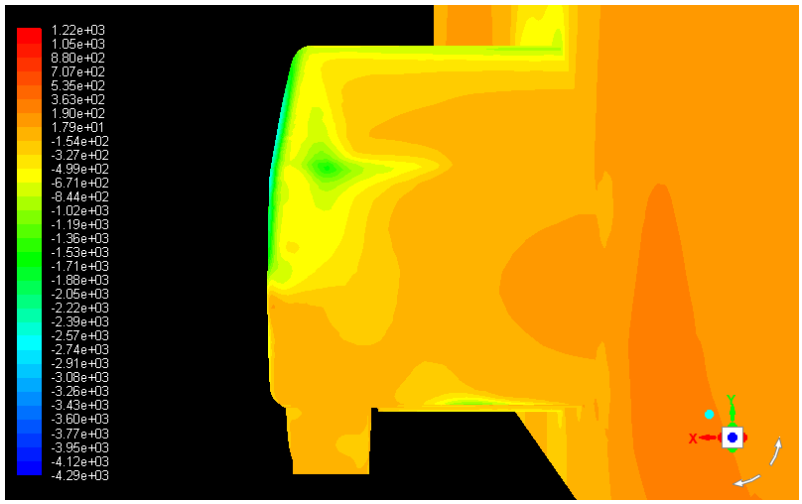

(a)

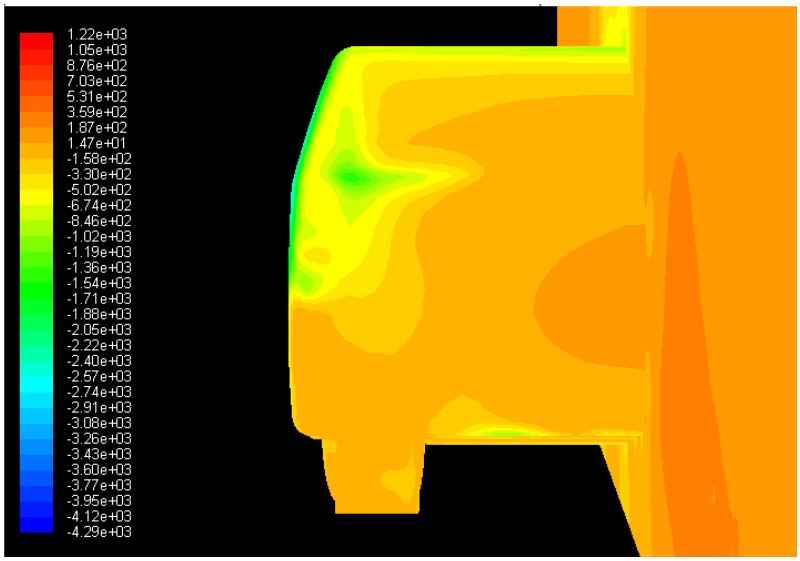

(b)

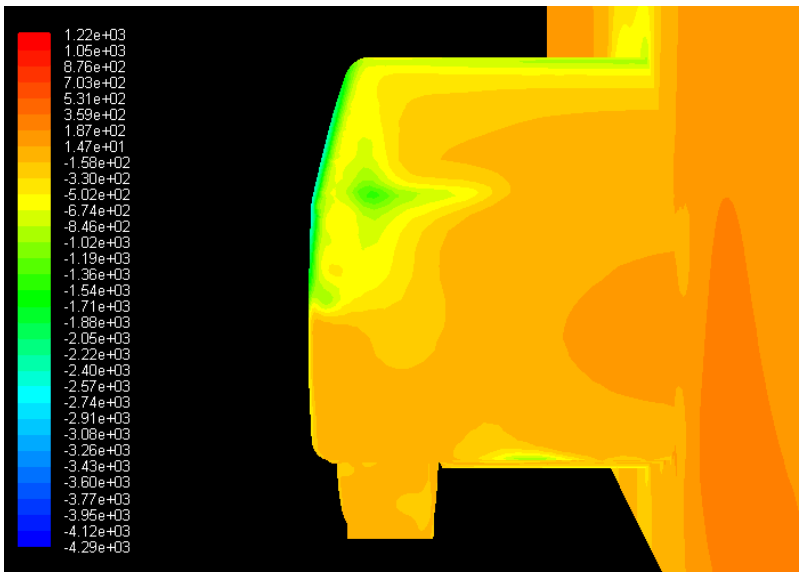

(c)

Figure 14. Static pressure distribution in the back of (a) M-W1, (b) C1-W1 and (c) C2-W1.

Overall, the results support the work of Buscariolo [13], who showed that substituting mirrors with cameras in an SUV resulted in a reduction in drag counts. The results also support the work of Olsson [10] and Magazoni [11], demonstrating the reduction in pressure at the rear of the vehicle due to changes in mirror shape.

Case 2 – Changing Wheel's Area while the Default Mirror Remains Unchanged

The vehicle was fitted with the two different wheel designs (W2 and W3) for the default mirror (M), and simulations were run in the second case. As mentioned in the geometry part, W1 is the standard design with a 25% coverage area, while W2 and W3 are modified derivatives of W1 that have coverage areas of 66% and 87%, respectively. Finally, the results are tabulated and compared, as can be seen in Table 6 and Figure 15.

Table 6. Variation in drag force with wheel coverage area for the default mirror

Configuration	Drag coefficient	Drag forces (N)	Reduction
M-W1 (baseline)	0.413	584	-
M-W2	0.408	578	1.0%
M-W3	0.402	568	2.7%

Figure 15 shows that W1 with a 25% coverage area causes the highest drag, and the drag reduces with the increase in the coverage area. Figures 16(a) to 16(c) show the static pressure distribution on the vehicle's back due to different wheels. Here, it can be observed that the high-pressure region in the back (marked by the darkest shade) is smallest in M-W1, more prominent in M-W2, and most considerable in M-W3. Therefore, the pressure difference is lesser as the coverage area increases, decreasing pressure drag and drag coefficient.

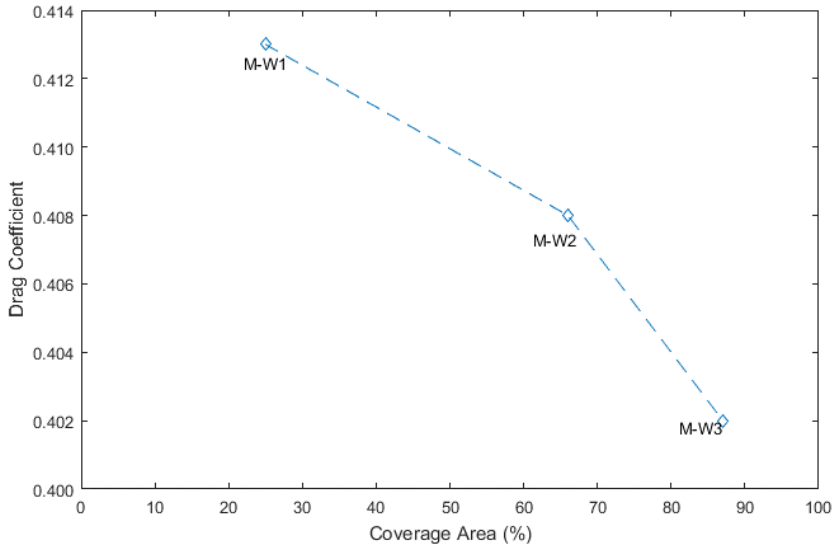

Figure 15. Change in drag force with wheel coverage area.

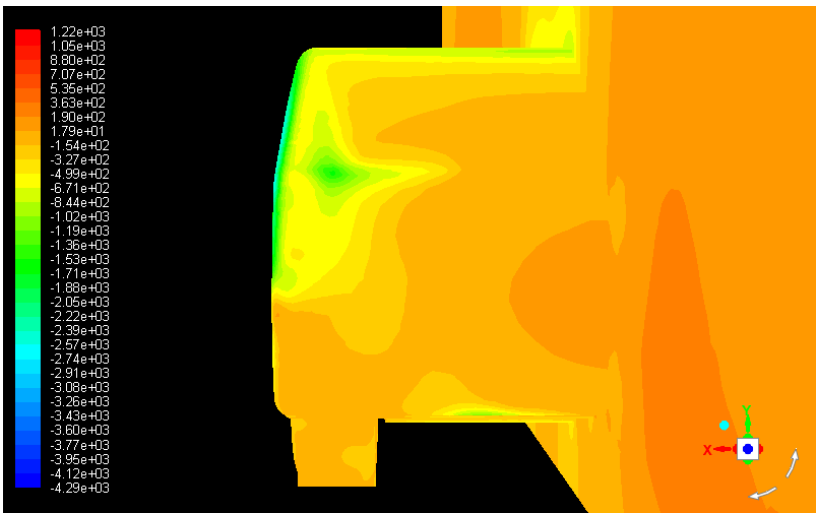

(a)

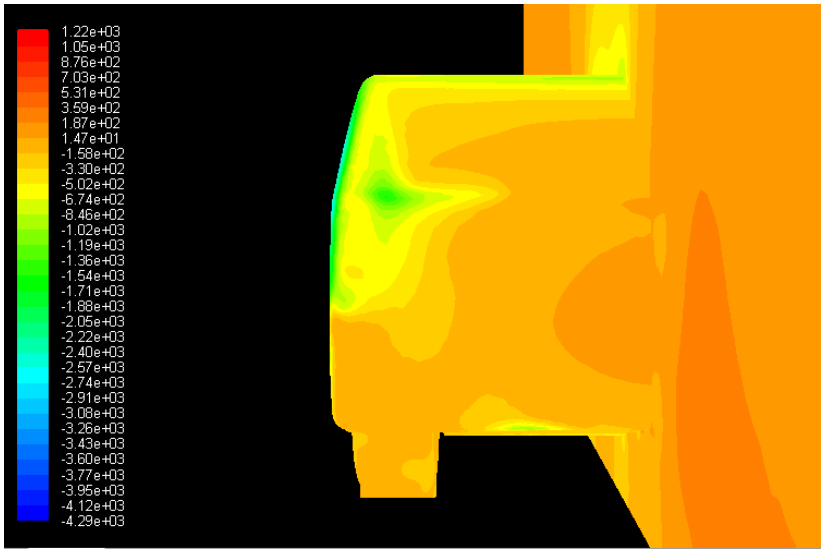

(b)

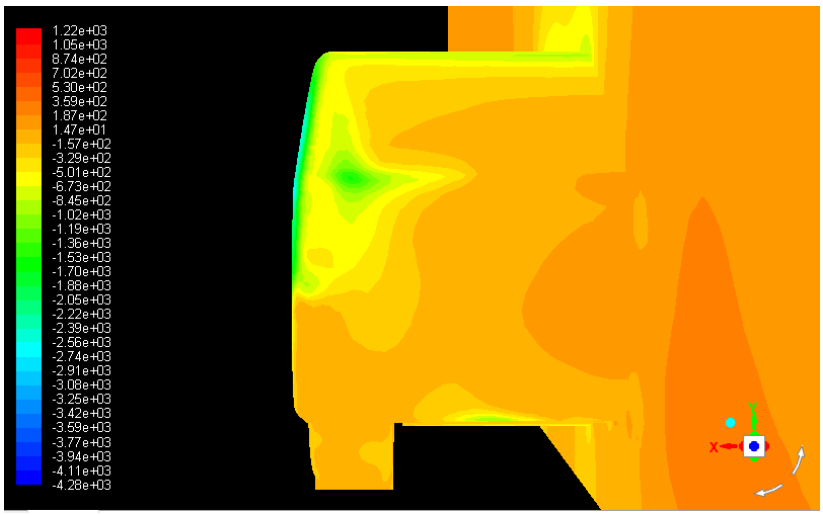

(c)

Figure 16. Static pressure distribution in the back of (a) M-W1 (note- same as Figure 14(a)), (b) M-W2, and (c) M-W3.

Finally, Figure 17(a) to 17(c) show the wake formation due to the different wheels. It was observed that W1 causes a relatively large wake past the front wheels and a wake inside the wheels between the rims. In the case of W2, the wake past the front wheels is slightly reduced. However, the wake in the front wheel itself is noticeably less. W3 has a substantial reduction in both wakes past the front wheel as well as the rims. In the rear wheels, the changes are relatively

straightforward. With an increase in coverage area, the wake areas in the wheel are reduced, causing less wake formation inside the wheel rims. From these pictures, it is evident that a higher wheel coverage area reduces wake formation overall, thereby contributing to drag reduction.

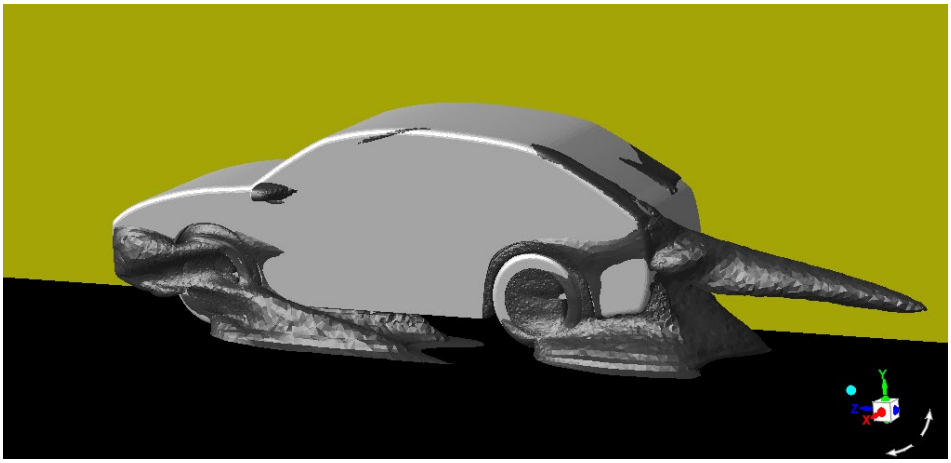

(a)

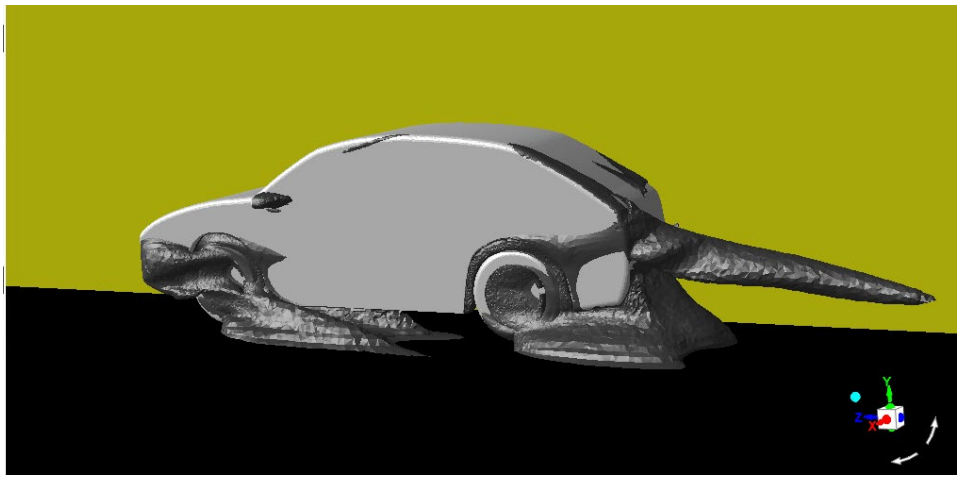

(b)

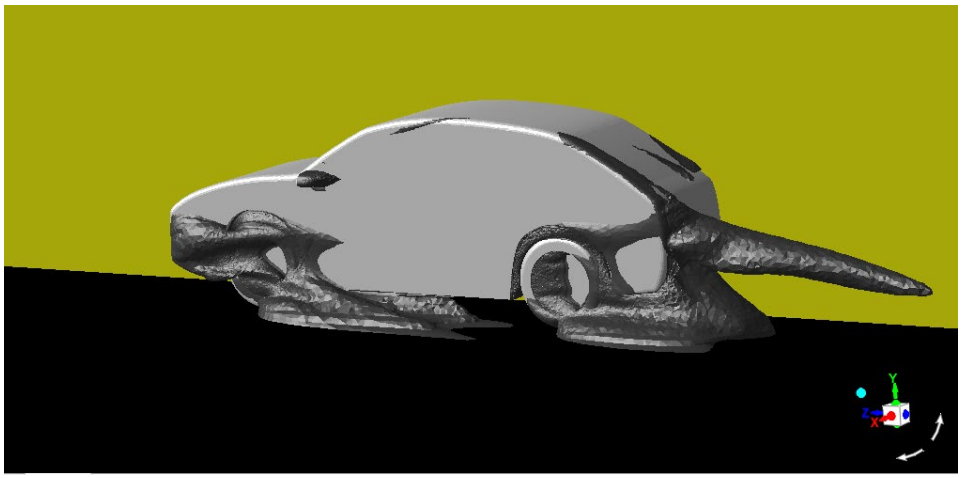

(c)

Figure 17. Iso-surface of wake formations in (a) M-W1, (b) M-W2, and (c) M-W3.

The obtained values are similar to the experimental results obtained by Bolzon et al. [6], who showed that the difference between 30% and 80% covered wheels is about 14 drag counts. The results also support Waschle [4], who showed that closed rims (i.e., 100% covered wheels) produce less drag than conventional wheels. From the two cases, it was found that C2 and W3 are the most significant modifications in terms of drag reduction. Hence, a new configuration C2-W3 was simulated. The drag forces and coefficient obtained are compared with those of other configurations, as illustrated in Table 7.

Table 7. Results of all tested configurations.

Configuration	C_d	Drag forces (N)	Percentage reduction in drag force
M-W1	0.413	584	-
M-W2	0.408	578	1.0%
C1-W1	0.409	574	1.7%
C2-W1	0.407	569	2.6%
M-W3	0.402	568	2.7%
C2-W3	0.399	559	4.3%

From Table 7, it is evident that, as expected, camera C2 and wheel W3 combination results in the highest reduction in drag force and drag coefficient compared to other combinations. The percentage reduction in drag force for the C2-W3 combination was found to be 4.3%.

CONCLUSION

The study was carried out to maximize aerodynamic efficiency using external modifications on side-view cameras and aerodynamic wheel covers. To achieve this goal, CFD-based numerical simulations were performed to determine the relative effect of these modifications on the drag coefficient reduction. The results can be summarized as follows:

i. The drag decreases with a reduction in the frontal area of the camera. Replacing mirrors with smaller cameras alone results in a substantial reduction in drag.
ii. The drag decreases with an increase in the coverage area of the wheels. A coverage area of 85-90% reduced the drag by 2.7%.
iii. A combination of smaller cameras and wheels with broader coverage areas needs to be used as this combination is found to have the most significant impact on the reduction in drag.
iv. This study used a simplified vehicle with a fixed wheel to ascertain the relative effect of external modification of camera/mirror and wheel covers on reducing the drag. However, to obtain more accurate results, a moving wall can be used in future to simulate the relative movement of the vehicle with the road as the flow around the wheels interacts significantly with the boundary layer of a moving road and vehicle underbody. Furthermore, transient simulation can be performed to examine the flow field's unsteady characteristics like vortex shedding.

REFERENCES

[1] G. Wickern, K. Zwicker, and M. Pfadenhauer, "Rotating wheels - their impact on wind tunnel test techniques and on vehicle drag results," SAE Technical Paper Series, 1997, doi: 10.4271/970133.

[2] L. Haag, T. Blacha, and T. Indinger, "Experimental investigation on the aerodynamics of isolated rotating wheels and evaluation of wheel rotation models using unsteady CFD," *Int. J. Automot. Eng.*, vol. 8, no. 1, pp. 7–14, 2017, doi: 10.20485/jsaeijae.8.1_7

[3] H. Berg and A. Brandt, "Investigation of aerodynamic wheel design", Master's thesis, Chalmers University of Technology, Sweeden, 2018.

[4] A. Wäschle, "The influence of rotating wheels on vehicle aerodynamics - numerical and experimental investigations," SAE Technical Paper Series, 2007, doi: 10.4271/2007-01-0107

[5] K. Sofie, G. Adrian and O. Gianluca, "An investigation of wheel aerodynamic effects for a saloon car", In: *10th FKFS Conference, Stuttgart, Germany*; 29-30 September, 2015.

[6] M. D. Bolzon, S. Sebben, and A. Broniewicz, "Effects of wheel configuration on the flow field and the drag coefficient of a passenger vehicle," *Int. J. Automot. Technol.*, vol. 20, no. 4, pp. 763–777, 2019, doi: 10.1007/s12239-019-0072-1

[7] W.-H. Hucho and S. R. Ahmed, *Aerodynamik des automobils eine brücke von der Strömungsmechanik zur Fahrzeugtechnik.* Berlin: Springer, 2013.

[8] G. J. Ehlert, R. J. Chapman, and R. S. Thomas, "Wind noise and aerodynamic drag optimization of outside rear view mirrors," *SAE Technical Paper Series*, 1993, doi: 10.4271/931292.

[9] S.Alam and S.M.Mahmood, "Study of side view mirrors design on the fuel consumption of a car," *Global Sci-Tech*, vol 6, no. 4, pp. 224-227, 2014. ISSN: 0975-9638

[10] M. Olsson, "Designing and optimizing side-view mirrors," Master's Thesis, Chalmers University of Technology, Sweeden, 2011.

[11] F. Magazoni *et al.*, "Aerodynamic shape improvement for driver side view mirror of hatchback vehicle using adjoint optimization method," SAE Technical Paper Series, 2015, doi: 10.4271/2015-36-0156

[12] D. Ipci, "A comparative CFD study of side-view mirror and side-view camera usages on a city bus," *International Journal of Automotive Science And Technology*, pp. 138–143, 2020, doi: 10.30939/ijastech..726376

[13] F. F. Buscariolo and V. Rosilho, "Comparative CFD Study of outside Rearview Mirror Removal and outside rearview cameras proposals on a current production car," SAE Technical Paper Series, 2013, doi: 10.4271/2013-36-0298

[14] S. R. Ahmed, G. Ramm, and G. Faltin, "Some salient features of the time-averaged ground vehicle wake," SAE Technical Paper Series, 1984, doi: 10.4271/840300

[15] T. McWha, "Heavy-duty vehicle rear-view camera systems," *SAE Int. J. Commer. Veh.*, vol. 7, no. 2, pp. 500–513, 2014, doi: 10.4271/2014-01-2381

[16] T. B. Korkut and A. Goren, "Aerodynamic effect of wing mirror usage on the solaris 7 solar car and Demobil 09 electric vehicle," *Int. J. Automot. Mech. Eng.*, vol. 17, no. 2, pp. 7868–7881, 2020, doi: 10.15282/ijame.17.2.2020.06.0587